Journal of the Civil Engineering Forum, January 2026, 12(1):53-74
DOI 10.22146/jcef.22631
Available Online at https://jurnal.ugm.ac.id/v3/jcef/issue/archive

Seismic Fragility of Fixed and Flexible Base RC Bridge under Near-Fault Directivity Effects

Fahad Bin Khurshid*, Md Shafquat Izhar, Nazrul Islam, Nabeel Ahmed Khan, Mohd. Bilal Khan
Department of Civil Engineering, FE&T, Jamia Millia Islamia, New Delhi, INDIA
*Corresponding author: fkhurshid@jmi.ac.in

SUBMITTED 29 June 2025 **REVISED** 21 August 2025 **ACCEPTED** 26 August 2025

ABSTRACT Reinforced Concrete bridges are widely used in highway infrastructure due to their cost-effectiveness and structural redundancy. However, they are highly vulnerable to seismic hazards, particularly in near-fault regions where ground motions exhibit extreme intensity and short-duration energy pulses. Near-fault ground motions are characterized by high-energy velocity pulses with long periods, pulse-like waveforms, and significant peak values, which can lead to severe structural damage. As modern design practices shift toward performance-based design, the vulnerability of bridges under these different types of near-fault ground motions have become an emerging area of interest for researchers and designers. However, a common practice is to assume fixed-base conditions for bridge piers during vulnerability assessments, which may lead to inaccurate results. The effect of assuming fixed-base conditions on the vulnerability assessment of bridge piers remains an open question. This study presents a comprehensive comparative analysis of seismic damage propagation in a simply supported multi-span RC bridge subjected to near-fault pulse-like ground motions with directivity effects. The bridge is modeled under two distinct foundation conditions: fixed-base and flexible-base, with the latter incorporating soil-structure interaction through a pile group foundation. The analytical framework employs Incremental Dynamic Analysis to develop seismic fragility curves, offering a thorough evaluation of the system-level performance. The results reveal that SSI significantly alters the structural response, with median normalized changes of approximately 27% in drift and 30% in base shear. In some cases, the normalized drift demand increased by up to 76.8%, whereas the normalized base shear decreased by up to 51.1%, indicating substantial shifts in deformation and force distribution. These variations significantly affect the energy dissipation capacity of the bridge, which is essential for mitigating damage progression and enhancing seismic resilience.

KEYWORDS Damage assessment; Fragility analysis; Incremental dynamic analysis; Regression analyses; Soil-structure interaction.

1 INTRODUCTION

Bridges are vital components of infrastructure, and play key roles in transportation networks, emergency response systems, and economic activities. Their design and maintenance are critical in seismically active regions, particularly in near-fault (NF) areas. The necessity for robust bridge structures in these regions arises from their vulnerability to the unique seismic hazards linked to NFPL-GMs (Akkar and Moghimi, 2018).

NF ground motions (NF-GMs) are distinctive seismic phenomena occurring close to the epicenter, exhibiting unique features that critically influence structural response and design strategies. These motions are characterized by strong velocity pulses, fling steps, and forward directivity effects, all of which result from the rupture mechanics of fault movement. Among these, pulse-like ground motions (PL-GMs) are especially significant, often presenting a dominant, long-period velocity pulse in the time history. These pulses arise when the fault rupture propagates toward a site at velocities near the shear wave speed, concentrating a large amount of energy in a single direction and dramatically increasing the structural demand—particularly for systems whose natural period matches or is close to the pulse period (Zhai et al., 2013). Another defining feature is the "fling step", a permanent ground displacement caused by differential fault motion. This step imposes quasi-static deformation demands, especially on long-span structures spanning fault zones (Dreger et al., 2011). The forward directivity effect, on the other hand, occurs when the rupture and seismic wave propagation directions align, leading to wave-front amplification and a distinct large velocity pulse at the beginning of the shaking. This can impose sudden, high-intensity loading that poses critical design challenges, particularly for flexible or long-period structures (Yang et al., 2009). NFPL-GMs impose intense demands on structures due to their impulsive, short-duration energy release, posing a significant risk especially for reinforced concrete (RC) systems. RC buildings, particularly existing

or conventional configurations, are often not designed to withstand the velocity pulse effects inherent in NF records. The impulsive nature of these records, which concentrate a significant portion of seismic energy over a short duration, greatly amplifies structural demand. NFPL-GMs are known to impose higher deformation and force demands than far-field GMs, especially in structures whose natural periods align with or are half the dominant pulse period (Gazetas, 1982). Moniri (2017) reported that such GMs lead to larger displacement demands and early plastic hinge formation, increasing the likelihood of collapse. Beyond buildings, other systems like tunnel form buildings (TFBs) and concrete gravity dams also exhibit increased seismic demand under NFPL-GMs. A study from Behesthi Aval et al. (2018) found that pulse effects significantly increased story shear, inter-story drift, and localized damage in TFBs. Similarly, gravity dams demonstrated nonlinear responses influenced by directivity and pulse characteristics, leading to differential damage patterns (Huang, 2015).

Multi-pulse GMs, containing several high-intensity peaks, generally induce more severe structural damage than single-pulse or non-pulse events. These records exhibit elevated spectral velocities, which translate into greater inter-story drift demands—a key indicator of seismic vulnerability (Chen et al., 2023). The unique response characteristics of NFPL-GMs, particularly forward directivity, can cause early yielding and large inelastic deformations. Alavi and Krawinkler (2004) and Behesthi Aval et al. (2018) observed that such records are especially dangerous for buildings with longer periods or high flexibility. Large-span systems, like cable-stayed bridges, are especially sensitive to these pulses, with tower components absorbing the brunt of the seismic energy (Li et al., 2017; Moniri, 2017). Moreover, collapse probability is significantly elevated under NF conditions: Champion and Liel (2012)found a collapse probability of up to 6% over 50 years for structures exposed to PL records—well above that for comparable far-field cases. These advances underscore the necessity of incorporating NF-specific effects in performance-based earthquake engineering frameworks to improve risk-informed design, retrofit prioritization, and long-term resilience planning.

Extensive research has explored the effects of NFPL-GMs on various bridge types. Studies on seismic isolation (Bi and Hao, 2012), retrofitting (Fauzan et al., 2025), train-track-bridge interactions (Lai et al., 2024), and probabilistic seismic demand modeling (Bohara et al., 2025; Paudel et al., 2024; Spagnuolo et al., 2016) have consistently shown that forward directivity pulses increase the likelihood of damage, particularly for bridges near faults. Further investigations into skewed bridges (Mangalathu et al., 2019) and the behavior of train-bridge systems under different fault mechanisms (Yu et al., 2022) highlight that structural geometry and fault type significantly influence seismic vulnerability. More recent work has suggested using PGV/PGA ratios to classify NFPL-GMs and assess damage potential, indicating that GMs with higher ratios lead to greater structural damage (Baig et al., 2023; Baig et al., 2024).

Most of the studies on vulnerability assessment of bridges assume fixed-base conditions, thereby ignoring the effects of soil-structure interaction (SSI) in bridges supported by deep or flexible foundations (Najar et al., 2025; Zhan et al., 2024). This assumption overlooks the dynamic interaction between the superstructure and substructure, especially in soft or layered soil profiles. In reality, SSI can influence a structure's period, damping, and mode shapes, consequently altering both displacement and force responses during significant ground shaking (Güllü and Jaf, 2016; Güllü and Özel, 2020). Ignoring these effects can lead to non-conservative evaluations of seismic vulnerability, particularly in the context of NF-GMs where energy demand is highly concentrated. The interaction between soil and structure can either amplify or mitigate the seismic demands on the structure, making SSI indispensable for accurate assessment and design (Xiong et al., 2016). Comparative studies have been conducted to evaluate the differences in seismic response between fixed-base and flexible-base (including SSI) assumptions. These studies reveal that structures on flexible bases exhibit distinct dynamic characteristics compared to those on fixed bases. For instance, it has been observed that SSI generally results in an increase in fundamental periods due to the added flexibility and inertia from the soil, thereby altering the anticipated seismic response (Hokmabadi and Fatahi, 2016; Xiong et al., 2016). SSI can significantly influence inter-story drift and lateral displacements, particularly in high-rise structures or bridges constructed on soft soils. Increased lateral displacement and drift are often recorded due to the enhanced flexibility introduced by the soil (Visuvasam and Chandrasekaran, 2019). This effect is more pronounced in structures with flexible foundations compared to those with fixed bases. The interaction between soil and structure affects the distribution and magnitude of shear forces within the structure. Structures with flexible bases might experience altered base shear values, sometimes reducing the expected shear demand due to the damping effects provided by the soil (Bárcena and Esteva, 2007). The fundamental period of a structure is often increased due to SSI. This elongation of the period is a result of the additional flexibility provided by the soil, which changes the dynamic response characteristics of the structure. Accurate modeling of these changes is crucial for ensuring that the seismic design considers the potential shifts in resonance and associated risk (Xiong et al., 2016).

Despite significant advancements in understanding NFPL-GMs and seismic fragility analysis, several critical research gaps persist. Firstly, there is a lack of studies that integrate both the forward directivity effects of NFPL-GMs and SSI within a unified framework. While research has independently examined the demands induced by directivity and the effects of SSI, their combined impact remains underexplored, limiting the applicability of findings for infrastructure in NF zones with soft soils. Secondly, the prevalent use of single-pier idealizations in bridge modeling constrains dynamic accuracy. These models apply seismic forces directly to representative piers, neglecting pier-superstructure interactions, bearing characteristics, and load redistribution. This approach fails to accurately capture actual responses such as ponding effects and rotational deformation. Thirdly, fragility analyses typically focus on a single engineering demand parameter (EDP)—usually pier-top drift—while excluding force-based measures such as base shear. This limitation hinders evaluation across multiple performance criteria, particularly where force transmission influences failure modes. Finally, comprehensive system-level bridge modeling under NFPL-GMs remains necessary.

To bridge existing research gaps, this study conducts a comparative seismic vulnerability assessment of a simply supported multi-span RC bridge with fixed and flexible foundation conditions subjected to NFPL-GMs. It explores the combined effects of these GMs with forward directivity and SSI through a pile group foundation. Two structural configurations: one with fixed-base pier supports and another incorporating SSI using a nonlinear pile group foundation system are assessed for their vulnerability to NFPL-GMs. Both models are subjected to identical sets of NFPL-GMs, consisting of ten High Directivity (HD) and ten Low Directivity (LD) records classified based on the ratio of Peak Ground Velocity (PGV) to Peak Ground Acceleration (PGA) threshold.

2 STRUCTURAL MODELING

To assess the influence of soil–structure interaction (SSI) on the seismic response of reinforced concrete (RC) bridges, this study developed and analyzed two distinct foundation scenarios for the same bridge structure: one assuming a rigid, fixed-base condition and the other incorporating a flexible-base system supported by a pile group that includes nonlinear SSI effects. The selected bridge configuration exemplifies a standard simply supported RC highway bridge, commonly employed in areas with soft to medium soil, classified as Zone V in the seismic map of India (Bureau of Indian Standards, 2016). The pile foundation design incorporates practical engineering considerations, ensuring that the modeling assumptions accurately reflect real bridge systems. The comparative analysis was conducted using incremental dynamic analysis (IDA) combined with Nonlinear Time History (NLTH) simulations, applying a range of seismic intensities defined by different intensity measures (IMs). The structural performance was quantified through key engineering demand parameters (EDPs), namely pier-top displacement (drift) and base shear allowing for a comprehensive evaluation of seismic vulnerability.

Over the past decade, IDA along with fragility analysis has emerged as a core methodology for assessing structural vulnerability under seismic loads. IDA enables the evaluation of bridge performance by simulating the nonlinear dynamic behavior of the system across a progressively increasing range of ground motion (GM) intensities, while fragility functions estimate the probability of exceeding predefined damage thresholds as a function of GM severity—typically represented through IMs such as peak ground acceleration (PGA) and peak ground velocity (PGV). In recent years, these tools have been further refined by incorporating multi-IM approaches, energy-based performance indicators, and probabilistic formulations for SSI representation, thereby enhancing their predictive capabilities. The present study utilizes IDA results to develop fragility curves for both foundation configurations, which serve as a probabilistic framework for evaluating and comparing bridge performance. Detailed modeling strategies and validation procedures for both the superstructure and foundation systems are elaborated in the subsequent sections.

2.1 Bridge Layout and Geometric Characterization

To simulate realistic seismic behavior, this study adopts a detailed numerical model of a RC bridge system with fixed-base support, which has been previously validated through experimental observations reported by Izhar et al. (2024). Figure 1 illustrates the analytical representation of the fixed-base bridge model as constructed in the simulation environment and Figure 2 presents the schematic diagram of the bridge model.

The modeled bridge comprises a four-span configuration, where each span measures 27 meters in length. This arrangement results in a total bridge length of 108 meters, making it representative of medium-span highway bridges. The overall deck width is 7.5 meters, which aligns with standard two-lane configurations in national highway systems. The superstructure is simplified as a spine model, consisting of beam elements aligned longitudinally with the bridge centerline. This configuration incorporates a deck slab of uniform thickness (0.225 meters) and three longitudinal I-shaped girders that

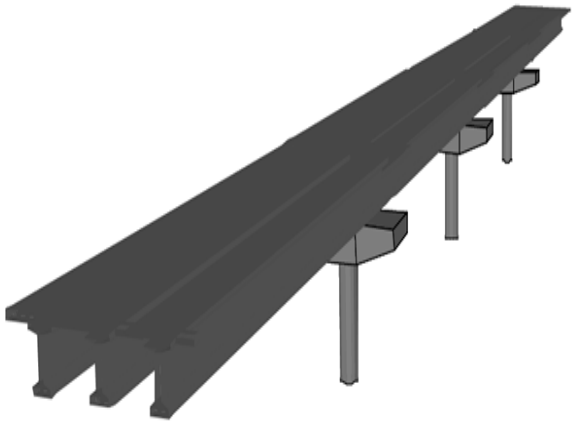

Figure 1 Finite element representation of RC Bridge with fixed-base support conditions.

support the deck. These girders are placed to ensure an even distribution of dead and live loads. The modeling philosophy captures the primary load path while maintaining computational efficiency.

To accurately capture the nonlinear characteristics of elastomeric bearings, which isolate the deck from the substructure, these elements were represented using nonlinear link components governed by bilinear hysteresis behavior. The hysteretic behavior was modeled using Kelly's idealization, which is particularly effective in simulating stiffness degradation and energy dissipation under cyclic loads (refer to Figure 3) (Naeim and Kelly, 1999). Where, K_1 is elastic stiffness in kN/m, K_2 is strain hardening stiffness (kN/m), K_{eff} is the effective stiffness (kN/m) and Q is the characteristic strength (kN). This treatment allows for reliable modeling of both the pre-yield and post-yield regimes of bearing response under seismic excitation.

The pier substructure consists of three RC columns, each having a circular cross-section with a diameter of 1.22 meters and a total structural height of 6.191 meters, measured from the foundation base to the pier cap top. To accurately represent their nonlinear flexural response, beam-column elements with distributed plasticity were used for pier modeling. This allows for a more precise capture of curvature demands and inelastic rotations, particularly under near-fault (NF) seismic excitations, which are characterized by strong velocity pulses and high energy content.

Table 1 presents a comprehensive summary of the bridge's geometric and structural configuration, integrating both previously tabulated and in-text parameters for completeness.

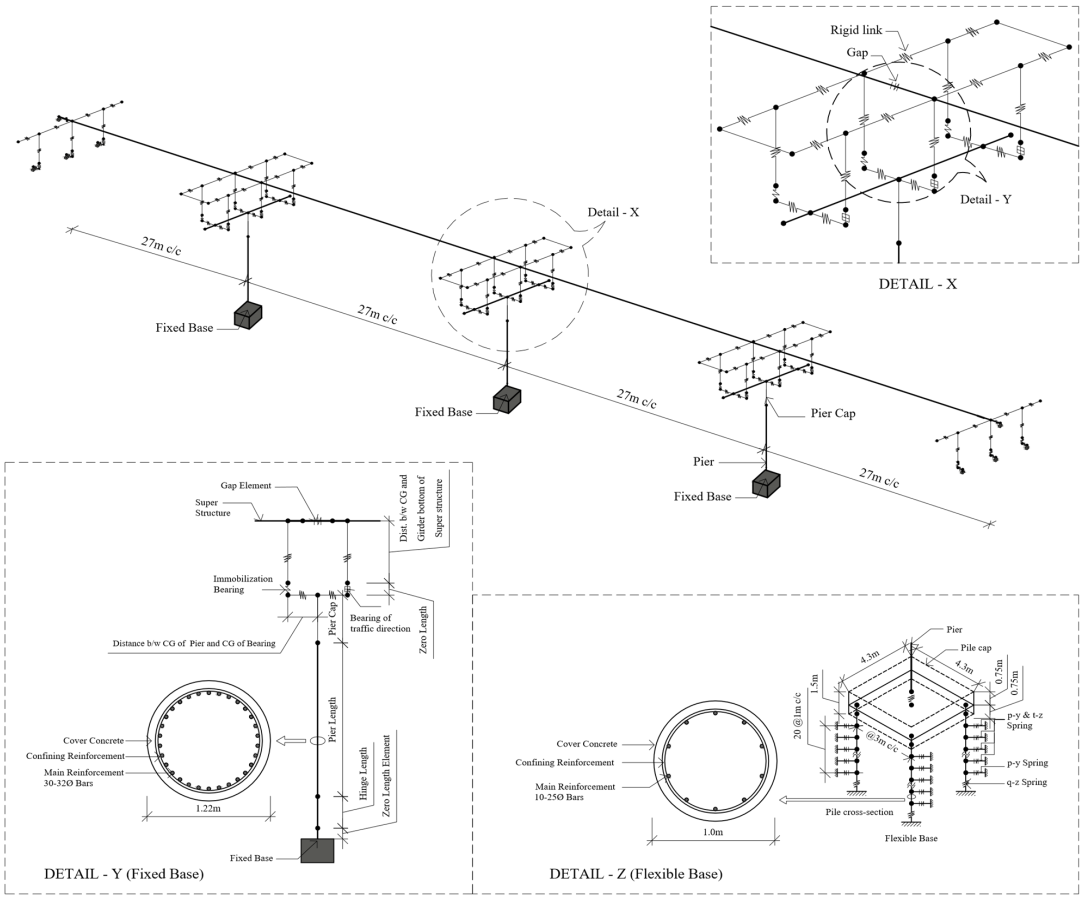

Figure 2 Schematic diagram of bridge assembly.

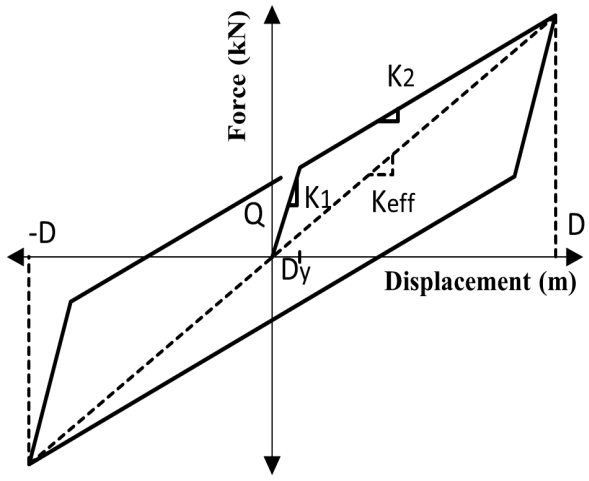

Figure 3 Bilinear hysteresis model for elastomeric bearing simulation (Naeim and Kelly, 1999).

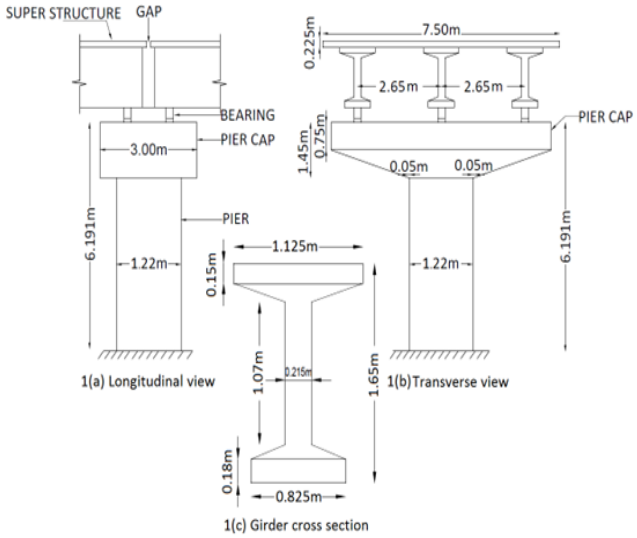

Figure 4 Schematic layout of bridge configuration.

2.2 Structural Idealization of the Superstructure

To accurately simulate the structural behavior of the bridge superstructure, the deck slab and longitudinal girders were modeled together as a monolithic composite system using frame-type elements. This modeling strategy was chosen to ensure that the global stiffness and mass characteristics of the girder-deck assembly are captured accurately. The entire superstructure was represented using a spine model approach, wherein beam elements were strategically positioned along the longitudinal centerline of the bridge, corresponding to the neutral axis of each composite section. Cross-sectional dimensions and stiffness parameters for all elements were derived based on the design prescriptions of the Indian Roads Congress guidelines (Indian Roads Congress, 2017; Izhar et al., 2024), ensuring that the model aligns with recognized national standards. The material configuration used for the bridge includes M40-grade concrete and Fe500-grade reinforcing steel, consistent across both the superstructure and substructure. The choice of these material grades ensures adequate ductility and compressive capacity to withstand high-intensity GMs, especially relevant in high seismic risk zones. The schematic presentation of the bridge superstructure is shown in Figure 4.

In terms of dynamic behavior, key mechanical properties such as Young's modulus, Poisson's ratio, and damping characteristics were assigned based on the Indian Standard codes and FEMA recommendations (Bureau of Indian Standards, 2016; FEMA356, 2000; FEMA695, 2009). These values were selected to maintain conformity with seismic design and performance evaluation practices.

Table 1. Key structural and geometric parameters of the simulated RC Bridge

Bridge Component	Parameter Description	Value/Range	Remarks
Span	Number	4	Equal-span layout
	Length (m)	27.00	
	Total bridge length (m)	108.00	
Deck and Super-structure	Overall width of bridge deck (m)	7.50	Two-lane configuration
	Deck slab thickness (m)	0.225	Uniform along the span
	Number of I-girders	3	Longitudinal girders supporting the slab
Bearings	Type and modeling	Elastomeric, bi-linear link	Kelly's hysteresis used
Sub-structure	Number of piers	3	Intermediate support structures
	Diameter of RC piers (m)	1.22	Circular cross-section
	Height of piers	6.191	From base to top of pier cap
Pier Cap	Depth of pier cap (m)	0.75 – 1.45	Tapered or variable-depth configuration

To represent energy dissipation mechanisms within the system under seismic excitation, Rayleigh damping was employed—a commonly adopted approach in structural dynamics (Alipour and Zareian, 2008). The damping parameters were calibrated to introduce 5% critical damping in the first two vibration modes, which is widely accepted for modeling RC systems subjected to earthquake loading (Alipour and Zareian, 2008). This damping ratio ensures that the model effectively simulates the expected hysteretic behavior and energy loss due to both material and structural damping under cyclic lateral loading.

2.3 Modeling of Piers and Bearings

The bridge piers were represented using fiber-based nonlinear beam-column elements, which provide an efficient yet accurate way to simulate distributed inelasticity across the pier cross-section. Each circular pier section was discretized into multiple fiber layers, enabling the model to capture local material nonlinearity under seismic forces. To reproduce the expected nonlinear flexural response during strong ground shaking, P-M_2-M_3 interaction hinges were assigned at the base of each pier. The plastic hinge length was calculated using an established empirical formula, refer to Equation (1), that takes into account the pier's geometry and material strength characteristics, ensuring appropriate modeling of curvature demands (Caltrans, 2010; Paulay and Priestley, 1992). This approach enables the capture of gradual stiffness degradation and strength loss as the pier transitions from elastic to inelastic behavior, which is critical for simulating damage progression during seismic events.

$$L_p = 0.08L + 0.022 f_{ye} d_b \quad \geq \quad 0.044 f_{ye} d_b \qquad (1)$$

Where, L_p is length of plastic hinge (mm), L is length of column (mm), f_{ye} is expected yield strength of longitudinal reinforcement (N/mm), and d_b is nominal diameter of longitudinal reinforcement (mm).

The bridge's elastomeric bearings were modeled based on their nonlinear force-deformation characteristics, including essential parameters such as initial stiffness, post-yield stiffness, yield strength, and deformation capacity (Naeim and Kelly, 1999; Roeder et al., 1987). These bearings were engineered to permit longitudinal movement along the bridge axis, accommodating thermal and seismic displacements, while restraining movement in the transverse and vertical directions to maintain structural stability. The directional control offered by these bearings plays a key role in limiting torsional responses and ensuring that the superstructure behaves predominantly in the intended lateral direction under seismic excitation. A summary of the mechanical and geometric properties used for the bearing elements is presented in Table 2.

Table 2. Configurational and mechanical specifications of modeled elastomeric bearings

Category	Property	Specification
Geometry	Plan Dimensions	500 mm × 500 mm
	Height	120 mm
Stiffness Values	Elastic Stiffness	6250.00 kN/m
	Effective Initial Stiffness	2500.00 kN/m
	Post-yield Stiffness	2083.50 kN/m
Deformation	Yield Displacement	12 mm
	Maximum Displacement Capacity	120 mm
Strength	Characteristic Strength	41.67 kN

2.4 Modeling of Foundation Conditions and Support Systems

To comprehensively analyze the seismic response of the bridge structure, the study considered two contrasting boundary support configurations: one assuming a fully restrained (fixed-base) condition and the other incorporating a flexible-base system that reflects realistic ground-structure interaction.

In the fixed-base scenario, the base of each pier was modeled as completely immobile, prohibiting any translation or rotation. This assumption implies a perfectly rigid connection to the supporting ground, thereby excluding the effects of soil compliance. While this simplification is commonly used in preliminary bridge design due to ease of modeling, it can significantly misrepresent seismic demands, especially for bridges founded in soft or stratified soil environments (Atefatdoost et al., 2018). The rigid-base assumptions tend to amplify internal forces, as it neglects damping and period-lengthening effects introduced by soil deformability, which are critical in seismic zones.

On the other hand, the flexible-base configuration was developed to offer a more realistic simulation of foundation behavior, by explicitly modeling cast-in-place RC piles beneath each pier. Specifically, each pier was assumed to rest on a pile group composed of four RC piles, each with a diameter of 1 meter and a length of 21 meters, arranged in a square layout with 3-meter center-to-center spacing in both longitudinal and transverse directions. This layout reflects practical design patterns and enables efficient load transfer to the soil medium. A summary of the key geometric and modeling parameters for this pile group system is provided in Table 3.

Table 3. Summary of geometric and modeling parameters for pile group foundation system

Parameter	Value	Description
Number of piles per group	4	2×2 square arrangement beneath each pier
Pile diameter	1.0 m	-
Pile length	21.0 m	Embedded in stratified soil
Pile spacing	3.0 m (c/c)	Equal spacing in both longitudinal and transverse axes
Pile cap thickness	1.5 m	-
Pile cap overhang	0.15 m	Extension beyond outer pile edges in all directions
Rigid link length (pier to cap)	0.75 m	Half of cap thickness to model vertical connection
Rigid link DOFs	6	3 translational + 3 rotational

The pile group was embedded in a layered soil profile, modeled to represent field conditions at seismically active sites. A reinforced concrete pile cap was placed atop each group for structural integration. The cap was designed with a thickness of 1.5 meters and extended 150 mm beyond the outermost piles in all directions. This overhang ensured adequate confinement and optimized force distribution from the pier to the foundation. The extended pile cap footprint also reduces local shear concentrations and improves bending performance by enlarging the effective transfer area.

For numerical modeling, the pile cap was represented using shell elements in SAP2000. These were finely meshed into 500 mm × 500 mm segments to accurately capture local stress gradients and deformation patterns. The shell model was located at the mid-depth of the cap to better reflect its stiffness and load path. To ensure accurate connectivity, rigid linear links were introduced between each pier base and the pile cap. These links were modeled as rigid link constraints across all six degrees of freedom (three translations and three rotations), thereby replicating a monolithic joint between the pile cap and the pier. The length of each link was set to half the thickness of the cap, thereby preserving geometric and mechanical compatibility across the connection.

This approach allowed pier forces to be transmitted efficiently into the foundation without introducing artificial flexibility or eccentricity at the interface. A visual depiction of the bridge configuration with the modeled pile group foundation is presented in Figure 5.

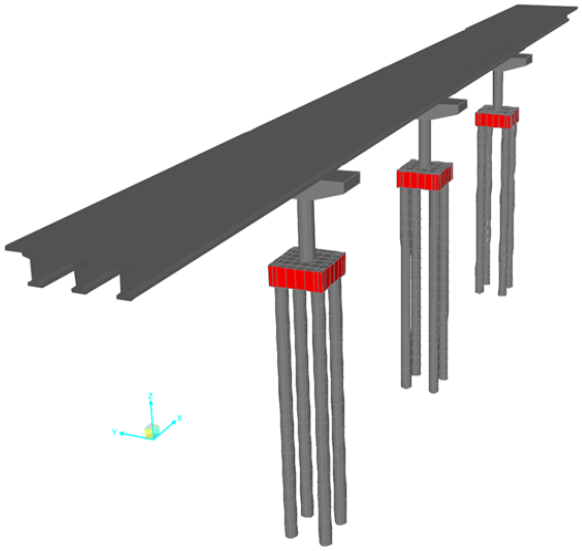

Figure 5 Numerical representation of bridge system with modeled pile group foundation.

2.5 Nonlinear Soil-Structure Interaction Modeling

The interaction between soil and the supporting pile group in the flexible foundation model was simulated using the Beam-on-Nonlinear-Winkler Foundation (BNWF) approach, a well-established method developed by Boulanger et al. (1999). In this framework, each pile is discretized into beam-column elements along its length, while the surrounding soil is represented using sets of nonlinear springs that capture realistic load-deformation behavior under dynamic conditions. To model the lateral resistance offered by the soil against pile deflection, $p{-}y$ springs were applied at discrete depths along each pile. These springs characterize the nonlinear lateral load-displacement behavior and vary with depth based on the overburden pressure and soil type. For simulating frictional resistance along the pile shaft, $t{-}z$ springs were included. These reflect shear transfer between the pile surface and adjacent soil layers. To account for end-bearing resistance at the pile tip, $q{-}z$ springs were utilized.

Each spring was modeled as a compression-only, gap-type zero-length element, allowing independent relative motion between the pile and the surrounding soil. The piles were divided into 1-meter segments, and at each node, a dual-nodded link element was used—one node attached to the pile and the other fixed in space to represent the static soil mass.

The upper part of the pile extended slightly above the ground surface, corresponding to half the depth of the pile cap, to match actual geometric boundary conditions. The vertical resistance at the base of the pile was represented using a $q{-}z$ spring element located at the tip. All spring properties, including ul-

timate resistance and deformation capacities, were derived from empirical relationships provided in the API (2000) guidelines (American Petroleum Institute, 2007).

As direct site-specific geotechnical data were unavailable, the study used representative soil data from previous research by Ajom and Bhattacharjee (2017), conducted in Assam, India—an area located in Seismic Zone V of the Indian seismic map. The site profile includes layers of medium sand (MS) and loose sand (LS) with varying stiffness and friction angles. Table 4 summarizes the representative soil profile characteristics adopted from geotechnical investigations conducted in Assam, India Ajom and Bhattacharjee (2017). These properties were used to calculate depth wise spring parameters for all piles, capturing the realistic nonlinear soil response under seismic excitation. The calculated nonlinear spring parameters at various depths are summarized in Table 5.

2.6 Validation of Soil-Structure Interaction Modeling

To ensure the reliability of the adopted SSI modeling approach, the results of a nonlinear pushover analysis for the present bridge model were benchmarked against findings from Mallick and Raychowdhury (2015). Their study investigated a similar RC bridge structure modeled under two boundary conditions: one assuming a fixed base and the other incorporating pile group foundations with SSI effects. In their analysis, the inclusion of SSI led to a marked reduction in base shear capacity, dropping from 8.2 MN (fixed base) to 6.7 MN (with SSI), corresponding to an 18% reduction. This behavior is attributed to the increased flexibility introduced by the soil–pile system, which enhances energy absorption and reduces peak lateral demands.

A similar modeling strategy was implemented in the current study using a BNWF model in SAP2000. The resulting pushover curves showed comparable trends. Specifically, the peak base shear reduced from approximately 4900 kN (fixed base) to 4300 kN (with SSI), reflecting a 12.25% decrease in lateral strength. Although the absolute values differ due to

Table 4. Soil Properties and Borehole Data (Ajom and Bhattacharjee,2017)

Depth (m)	Soil type	Frictional Angle	Saturated unit weight (kg/m^3)	Coefficient of lateral earth pressure, K	Void Ratio
1	MS	33.50	1640	0.45	0.70
2	MS	32.00	1500	0.47	0.77
3	MS	35.00	1810	0.43	0.65
4	LS	31.00	1440	0.48	0.85
5	MS	33.50	1640	0.45	0.70
6	MS	33.50	1570	0.45	0.70
7	MS	33.50	1590	0.45	0.70
8	MS	33.50	1620	0.45	0.70
9	LS	31.00	1460	0.48	0.85
10	MS	32.00	1460	0.47	0.77
11	MS	32.00	1610	0.47	0.77
12	MS	32.00	1520	0.47	0.77
13	MS	32.00	1550	0.47	0.77
14	MS	32.00	1600	0.47	0.77
15	MS	33.50	1580	0.45	0.70
16	MS	33.50	1600	0.45	0.70
17	LS	31.00	1560	0.48	0.85
18	MS	32.00	1520	0.47	0.77
19	MS	32.00	1600	0.47	0.77
20	MS	35.00	1910	0.43	0.65
21	MS	35.00	1890	0.43	0.65

Table 5. Strength and stiffness parameters for soil springs

Depth (m)	P_u (kN)	y_{50} (m)	t_u (kN)	z_{50} (m)	Q_u (kN)	z_{50} (m)
1	91.66	0.0039	23.52	0.0008	-	-
2	214.77	0.0065	39.37	0.0019	-	-
3	665.63	0.0077	79.54	0.0022	-	-
4	621.72	0.0122	72.93	0.0045	-	-
5	1262.94	0.0109	112.65	0.0038	-	-
6	1681.87	0.0121	129.41	0.0044	-	-
7	2260.14	0.0139	152.90	0.0052	-	-
8	2949.59	0.0159	189.91	0.0064	-	-
9	2739.20	0.0238	173.72	0.0107	-	-
10	3566.33	0.0215	209.48	0.0099	-	-
11	4708.22	0.0258	254.10	0.0120	-	-
12	5242.78	0.0263	261.71	0.0124	-	-
13	6226.65	0.0288	289.11	0.0137	-	-
14	7405.37	0.0319	307.72	0.0145	-	-
15	9462.63	0.0272	325.58	0.0110	-	-
16	10849.08	0.0292	375.12	0.0127	-	-
17	8325.16	0.0383	350.61	0.0215	-	-
18	9662.46	0.0323	392.56	0.0185	-	-
19	10736.06	0.0340	399.06	0.0188	-	-
20	20236.07	0.0349	501.44	0.0136	-	-
21	21025.38	0.0346	-	-	2752	0.013

variations in geometry, material properties, and site conditions, the consistent reduction trend validates the effectiveness of the SSI modeling framework.

Beyond base shear reduction, the change in the system's fundamental time period further validates the influence of foundation flexibility. In the study by Mallick and Raychowdhury (2015), the natural time period increased from 0.52 s (fixed base) to 0.95 s (flexible base) — an 82.69% increase. In the present study, a similar shift was observed: the time period increased from 0.56 s to 0.94 s, indicating a 67.86% rise. This increase reflects the reduction in overall system stiffness due to soil compliance and is a hallmark indicator of effective SSI representation. The comparative results are presented in Table 6.

Table 6. Comparison of fundamental natural time periods

Study	Fixed Base (s)	Flexible Base (s)	Change (%)
Mallick and Raychowdhury (2015)	0.52	0.95	82.69
Present Study	0.56	0.94	67.86

3 NONLINEAR MATERIAL MODELING AND PERFORMANCE LIMIT STATES

To realistically simulate the nonlinear behavior of RC bridge piers under seismic excitation, a detailed fiber-based modeling approach was implemented in this study. Each circular pier cross-section was discretized into a large number of fiber cells, with each cell assigned material-specific nonlinear stress–strain properties. The section was divided into three key material regions: confined concrete, typically located within the core of the section enclosed by transverse reinforcement; unconfined concrete, generally found in the outer cover region; and longitudinal steel reinforcement. These fibers enabled a localized representation of inelastic behavior across the section and provided an effective framework for tracking damage progression under cyclic loads.

To capture the distinct behavior of confined and unconfined concrete, strain-based damage thresholds were defined and used as performance indicators. Three strain limits were adopted—two for unconfined concrete to identify cracking and crushing, and one for confined concrete to mark the onset of significant core degradation. These strain values, presented in Table 7, serve as the basis for defining performance states such as yielding, spalling, or loss of lateral load capacity.

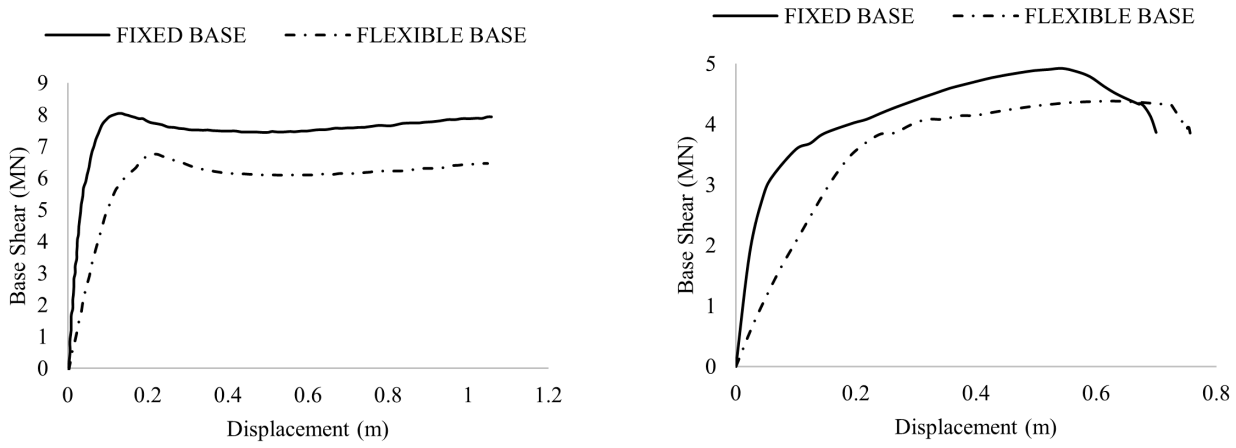

(a) (b)

Figure 6 Comparison of pushover responses for bridge system with and without SSI: (a) Reference study by Mallick and Raychowdhury (2015); (b) Present study.

This separation between concrete regions is essential in seismic fragility assessments, allowing the model to identify where and when failure initiates within the cross-section.

Where, ε_{utu} is ultimate tensile strain of cover concrete, ε_{cover} is strain in cover concrete, ε_{ucu} is ultimate compressive strain of unconfined concrete, ε_{sy} is yield strainof main longitudinal bars, ε_s is strain in main longitudinal bars, ε_{bb} buckling strain of main longitudinal bars, ε_{core} is strain in core concrete, and ε_{ucc} is ultimate compressive strain of confined concrete.

The longitudinal steel reinforcement was modeled using a nonlinear constitutive law that includes yielding, post-yield hardening or degradation, and possible bar buckling, particularly under high compressive strain demands. Two critical strain limits were used for steel fibers: ε_{sy} and ε_{bb}. The latter was determined using an empirical relationship described in Equation (2) and based on well-established formulations (Goodnight et al., 2015). The material characteristics in the model correspond to M40-grade concrete and Fe500-grade reinforcing steel, with longitudinal reinforcement consisting of thirty 32-mm-diameter bars distributed evenly throughout the cross-section.

$$\varepsilon_{bb} = 0.03 + 700\rho_s \frac{f_{yhe}}{E_s} - 0.1\frac{P}{f_{ce}A_g} \qquad (2)$$

Where, f_{yhe} is yield stress of confining steel (N/mm^2), P is axial load on pier (kN), f_{ce} is expected compressive strength of concrete (N/mm^2), and A_g is gross area of pier cross-section (mm^2)

NLTH analysis was conducted using the Takeda hysteresis model, which is well-suited for capturing the cyclic response of RC elements (Takeda et al., 1970). The model incorporates stiffness degradation, strength deterioration, pinching behavior, and residual deformation observed in RC components subjected to repeated loading and unloading. Its application here is particularly appropriate for simulating pier behavior in NF seismic environments, where structures are prone to large inelastic excursions and energy dissipation is a key aspect of performance. The Takeda model's ability to replicate experimental hysteresis in RC members with limited detailing enhances the accuracy of the simulation, especially in fiber-based modeling frameworks used for seismic fragility and performance assessment.

Table 7. Damage states (Izhar et al., 2024)

Damage States	Strain Limits	Description
Slight	$\varepsilon_{utu} \leq \varepsilon_{cover} < \varepsilon_{ucu}$ and $\varepsilon_{sy} \leq \varepsilon_s \leq \varepsilon_{bb}$	Cracking of cover concrete and yielding of main longitudinal bars
Moderate	$\varepsilon_{cover} > \varepsilon_{ucu}$ and $\varepsilon_{sy} \leq \varepsilon_s < \varepsilon_{bb}$	Spalling of unconfined/cover concrete
Extensive	$\varepsilon_s \geq \varepsilon_{bb}$ and $\varepsilon_{core} < \varepsilon_{ucc}$	Buckling of main longitudinal bars
Collapse	$\varepsilon_{core} \geq \varepsilon_{ucc}$	Crushing of confined/core concrete

4 GROUND MOTION SELECTION FOR NONLINEAR TIME HISTORY ANALYSIS

To conduct a robust IDA, this study employed two carefully curated sets of NFPL-GMs exhibiting forward directivity effects. These sets represent low and high directivity conditions, and were sourced

Table 8. Set of NFPL-GMs exhibiting LD

Earthquake name	RSN	M_w (Mag)	R_{rup} (km)	PGA (g)	PGV (cm/s)	PGV:PGA (cm/s/g)
Imperial Valley-06	180	6.53	3.95	0.53	48.91	94.31
Imperial Valley-06	181	6.53	1.35	0.45	67.02	152.74
Loma Prieta	802	6.93	8.50	0.51	41.58	82.39
Northridge-01	1004	6.69	8.44	0.75	77.67	105.22
Northridge-01	1052	6.69	7.26	0.30	30.81	104.22
Northridge-01	1054	6.69	7.46	0.55	76.07	139.11
Kobe_Japan	1119	6.90	0.27	0.70	68.41	99.99
Bam_Iran	4040	6.60	1.70	0.81	124.12	156.66
Montenegro_Yugoslavia	4451	7.10	6.98	0.37	41.24	112.88
Darfield_New Zealand	6906	7.00	1.22	0.77	116.10	154.81

Table 9. Set of NFPL-GMs exhibiting HD

Earthquake name	RSN	M_w (Mag)	R_{rup} (km)	PGA (g)	PGV (cm/s)	PGV:PGA (cm/s/g)
Imperial Valley-06	171	6.53	0.07	0.32	72.95	234.44
Imperial Valley-06	184	6.53	5.09	0.35	75.58	218.48
Superstition Hills-02	723	6.54	0.95	0.43	134.29	317.01
Landers	879	7.28	2.19	0.73	133.40	187.52
Northridge-01	982	6.69	5.43	0.41	111.47	276.79
Northridge-01	1013	6.69	5.92	0.43	74.84	178.96
Northridge-01	1045	6.69	5.48	0.42	118.18	287.25
Loma Prieta	3548	6.93	5.02	0.44	85.69	197.30
Darfield_New Zealand	6911	7.00	7.29	0.45	105.93	239.91
Darfield_New Zealand	6927	7.00	7.11	0.46	108.74	240.27

from the PEER NGA-West2 database, a widely recognized repository of recorded earthquake GMs. The classification into LD and HD was based on pulse strength, as indicated by specific velocity-to-acceleration criteria, and the selected motions are cataloged in Table 8 and 9, respectively (Pacific Earthquake Engineering Research Center, 1999).

The selection of GMs followed stringent selection criteria to ensure their relevance and severity for NF seismic scenarios. First, only records from sites with source-to-site distances (R_{rup}) less than 15 km were considered, to ensure strong near-field effects and minimize attenuation (Sharma et al., 2021). Second, the moment magnitude (M_w) of the events was required to exceed 6.5, ensuring that the selected motions are representative of major seismic events with sufficient energy release to significantly challenge structural performance (FEMA695, 2009). Third, and most importantly, the classification into LD and HD categories was governed by the ratio of PGV to PGA—a key indicator of pulse dominance in the velocity time history. Specifically, motions with PGV:PGA ratios less than 160 cm/s/g were categorized as NFPL-GMs with LD, while those with PGV:PGA ratios exceeding 160 cm/s/g were assigned to the HD group (Baig et al., 2024; Sharma et al., 2021).

This threshold is informed by prior research which suggests that a higher PGV:PGA ratio correlates with longer-period velocity pulses (Sharma et al., 2021)—indicative of stronger forward directivity—which can significantly influence the dynamic response of long-period structures such as bridges. This two-tier classification allows for a systematic investigation of how varying levels of NF pulse severity influence seismic demands and fragility outcomes for the RC bridge model considered in this study.

5 SELECTION OF APPROPRIATE INTENSITY MEASURES

The choice of a suitable IM is a critical step in accurately quantifying the seismic vulnerability of structures. The effectiveness of any IM is generally evaluated based on four criteria: efficiency, practicality, proficiency, and computability (Padgett et al., 2008). An optimal IM not only correlates strongly with structural demand but also enables consistent and repeatable vulnerability predictions across different GM records.

It has been widely accepted in literature that PGA serves as a reliable IM for most structures due to its simplicity and historical prevalence in design codes (Padgett et al., 2008). However, in the context of NF-GMs—especially those exhibiting pulse-like characteristics—PGV is considered to be a more effective descriptor of GM severity (Jiang et al., 2020). This is because PGV better captures the impulsive energy content and velocity pulses that dominate the structural response of long-period systems such as bridges. Consequently, many studies have recommended using both PGA and PGV for evaluating seismic vulnerability under such conditions (Baker, 2007; Billah et al., 2013; Izhar et al., 2024; Kabir et al., 2019).

In the present study, both PGA and PGV were employed as candidate IMs to comprehensively assess their performance under NFPL-GMs with FD, for both fixed-base and flexible-base (SSI-included) bridge configurations. This dual-IM approach allows for an informed comparison, where PGA captures short-duration intensity effects and PGV reflects pulse-dominated, long-period influences—offering insight into how different dynamic characteristics interact with structural response mechanisms. To evaluate the suitability of PGA and PGV as IMs, a regression analysis was performed using a power-law model, which establishes a logarithmic relationship between EDPs and the selected IMs. This relationship, mathematically expressed in Equation (3), is widely used for fragility model development due to its compatibility with the lognormal distribution assumptions typically used in vulnerability analysis (Billah et al., 2013; Padgett et al., 2008).

$$EDP = a(IM)^b \text{ or } \ln(EDP) = b\ln(IM) + \ln(a) \quad (3)$$

The regression was carried out using data obtained from the IDA performed under the suite of selected NFPL-GMs. The dispersion ($\beta_{EDP|IM}$), which reflects the scatter in the response at a given IM level,

Table 10. Regression parameters for NFPLGMs with forward directivity

EDP	Foundation	IM	*a*	*b*	β	ζ	R^2
Low Directivity							
Drift	Fixed Base	PGA	3.34	1.08	0.37	0.34	0.89
		PGV	0.06	0.96	0.55	0.57	0.77
	Flexible Base	PGA	4.65	1.12	0.37	0.33	0.90
		PGV	0.07	1.00	0.54	0.54	0.79
Base Shear	Fixed Base	PGA	7241.62	0.63	0.19	0.30	0.92
		PGV	671.83	0.57	0.27	0.47	0.83
	Flexible Base	PGA	6040.25	0.66	0.17	0.26	0.94
		PGV	498.90	0.60	0.25	0.42	0.87
High Directivity							
Drift	Fixed Base	PGA	4.93	1.22	0.41	0.34	0.89
		PGV	0.02	1.12	0.52	0.46	0.82
	Flexible Base	PGA	5.01	1.10	0.40	0.36	0.88
		PGV	0.04	1.03	0.48	0.47	0.81
Base Shear	Fixed Base	PGA	8674.13	0.67	0.14	0.21	0.95
		PGV	460.08	0.63	0.31	0.49	0.90
	Flexible Base	PGA	7923.59	0.74	0.20	0.27	0.96
		PGV	291.60	0.71	0.29	0.41	0.91

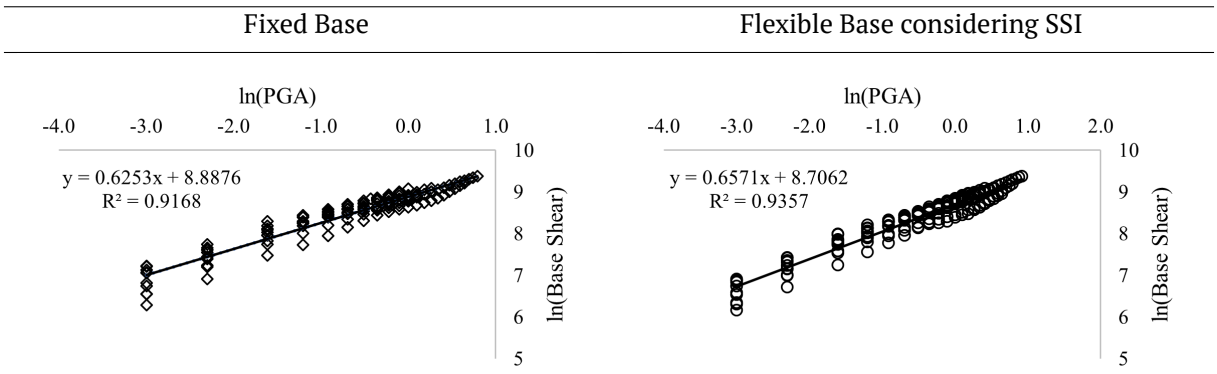

Figure 7 Regression trends showing PGA vs. Base Shear for fixed-base and SSI-based bridge models under NFPL-GMs with LD.

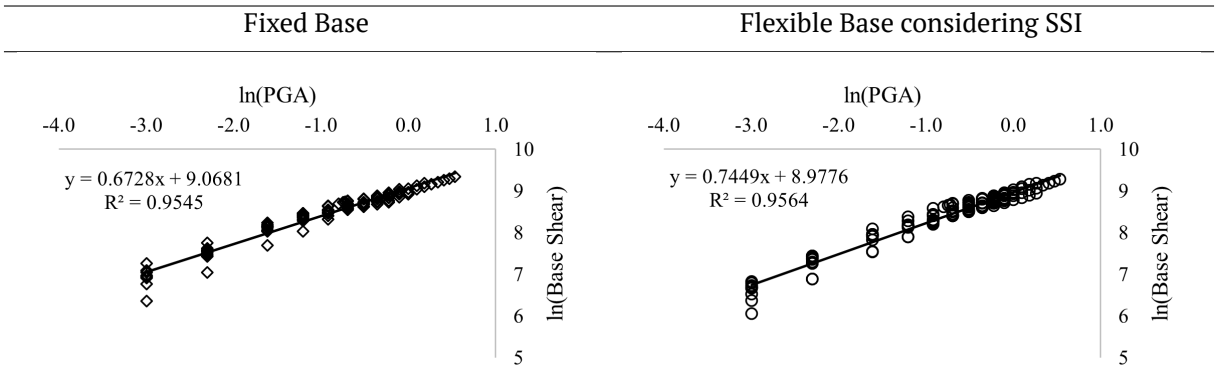

Figure 8 Regression trends showing PGA vs. Base Shear for fixed-base and SSI-based bridge models under NFPL-GMs with HD.

was computed using the conditional standard deviation of regression, as defined in Equation (4). A lower dispersion value indicates that the IM is more efficient, as it yields more consistent demand predictions across different GMs. In addition to efficiency, the regression slope coefficient *"b"* and constant *"a"* were used as an indicator of practicality, since a steeper slope implies greater sensitivity of the structural response to increasing intensity levels—an important feature for performance-based design (Padgett et al., 2008).

$$\beta_{EDP|IM} = \sqrt{\frac{\sum(\ln(EDP) - \ln(aIM^b))^2}{N-2}} \quad (4)$$

Where N is Total number of NLTH analyses. To consolidate these two criteria, a proficiency measure (ζ) was calculated, combining both dispersion and slope into a single indicator. A lower proficiency value implies that the IM is both statistically stable and dynamically relevant for predicting seismic demand. This formulation is presented in Equation (5), following prior studies (Billah et al., 2013; Izhar et al., 2024; Padgett et al., 2008).

$$\zeta = \frac{\beta_{EDP|IM}}{b} \quad (5)$$

The regression framework thus provides a rigorous, quantitative basis for selecting the most appropriate IM by evaluating not just correlation but also variability and predictive clarity across different response metrics. The logarithmic correlation between EDP "base shear" and the selected IM "PGA" is illustrated in Figure 7 and 8, and the regression parameters are presented in Table 10, for both fixed-base and flexible-base bridge models under forward-directivity NFPL-GMs.

The outcomes of the regression analysis provide a clear distinction in the performance of the two candidate IMs—PGA and PGV—when predicting structural response under NFPL-GMs with forward directivity. Across both the fixed-base and flexible-base (SSI-inclusive) configurations, PGA consistently outperforms PGV in terms of correlation strength, lower dispersion, and overall proficiency when used to estimate drift ratio and base shear. These trends hold true under both LD and HD GM scenarios, confirming that PGA remains a robust and efficient indicator of seismic intensity even when forward-directivity effects are present.

A particularly noteworthy result is the exceptional performance of base shear as an EDP. Regression relationships between PGA and base shear demonstrate minimal scatter and high R^2 values (up to

0.96), indicating a tight and reliable correlation. Unlike drift ratio, which can be more sensitive to local structural behavior or nonlinear deformation modes, base shear reflects the global force demand in the system and responds more uniformly to changes in GM intensity. This makes it not only an analytically reliable EDP, but also one that is practically measurable and less prone to interpretational variability.

The influence of SSI on regression behavior was also found to be surprisingly limited, with only minor changes in regression slopes (b) and dispersion (β) between the fixed and flexible base models. This outcome can be attributed to the moderately stiff soil profile, which does not introduce significant period elongation or nonlinear damping. As a result, the high-frequency content of GMs—well captured by PGA—continues to dominate the structural response, even in the presence of foundation flexibility. This observation aligns with prior studies noting that SSI effects become prominent primarily in soft or highly deformable soils, where rocking and radiation damping play a more critical role.

In summary, the regression analysis confirms that PGA is a more reliable and efficient IM for fragility-based assessment of RC bridges subjected to NFPL-GMs with forward directivity, particularly under the soil conditions considered in this study. At the same time, base shear emerges as a high-performing, yet often underutilized, EDP that offers strong correlation, low variability, and practical relevance. Its consistency across both base configurations and motion types reinforces its value in performance-based seismic evaluations. This justifies the focused use of PGA vs. base shear in regression plotting and further supports the inclusion of base shear as a primary decision-making parameter in seismic vulnerability studies.

6 DISCUSSION ON RESULTS

The seismic performance of the RC bridge was assessed using IDA, with PGA selected as the IM, drift ratio, and base shear considered as the primary EDPs. To conduct IDA, the initial PGA value for the GMs was set at 0.05 g. This value is then increased incrementally, starting from 0.1 g and rising in steps of 0.1 g to higher PGA values. IDA was conducted for both fixed-base and flexible-base models incorporating SSI, facilitating a comparative analysis of how foundation flexibility influences seismic responses across various damage states.

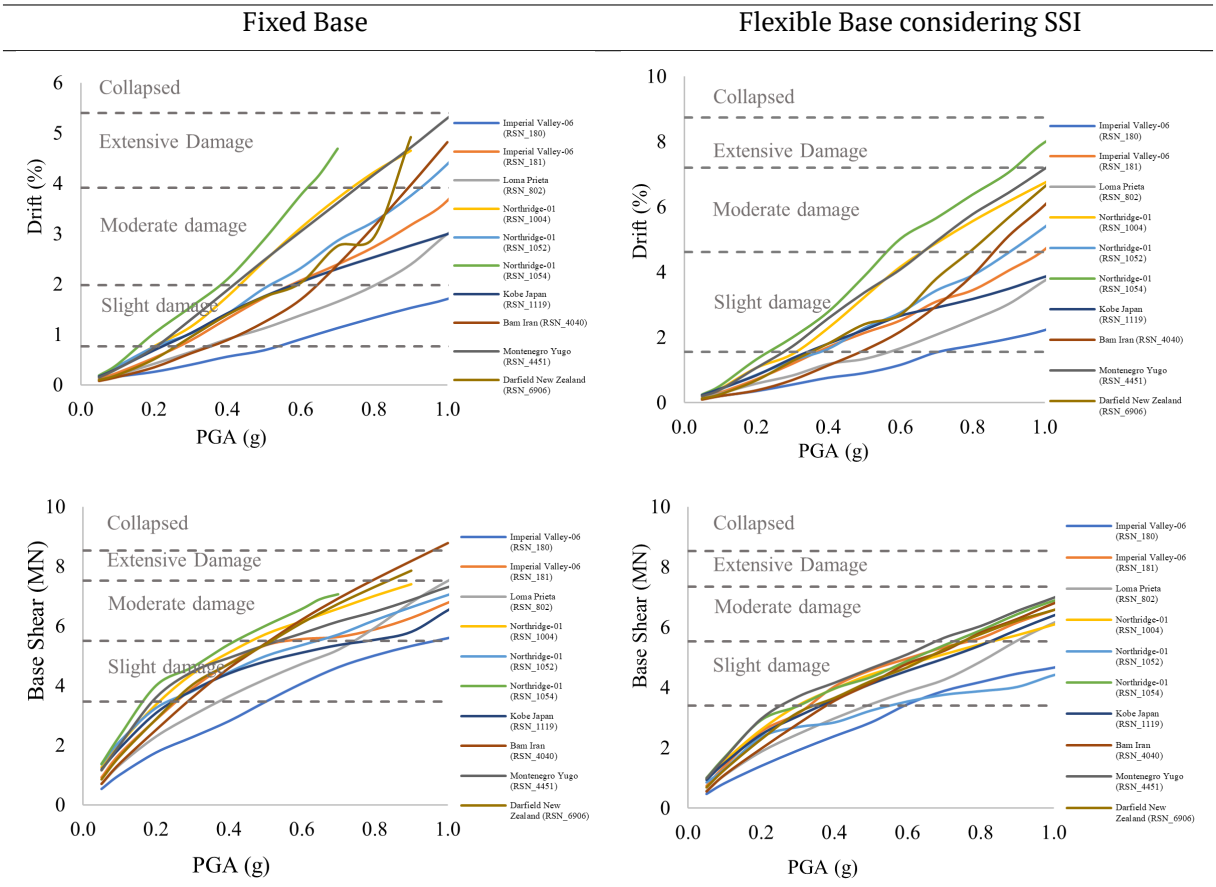

Figure 9 IDA curves of PGA versus drift and base shear under NFPL-GMs with LD.

6.1 NFPL-GMs with LD

A series of NFPL-GMs with LD were utilized to evaluate the seismic response of both fixed-base and flexible-base bridge models, with the latter incorporating SSI. Among the selected records, the Loma Prieta earthquake (RSN_802) exhibited the lowest PGV/PGA ratio, making it an exemplary case for capturing characteristic LD effects. Figure 9 presents the IDA curves for PGA versus drift and base shear for both models.

At the onset of slight damage, the fixed-base model exhibited distress at 0.30g PGA, corresponding to a drift of 0.65% and a base shear of 3003 kN. In contrast, the flexible-base model required 0.40g PGA to reach the same damage state, accompanied by a significantly larger drift of 1.18% and a slightly lower base shear of 2985 kN. This shift underscores the role of SSI in softening the structural response and reducing force transmission while increasing displacement demands. As the seismic intensity increased, the divergence in structural behavior became more pronounced. At moderate damage, the fixed-base system reached 1.65% drift and 5203 kN base shear at 0.70g PGA, whereas the flexible-base model required 0.90g PGA, with 3.02% drift and 5566 kN base shear. Although the flexible-base model absorbed a higher drift, it achieved a comparable or slightly higher base shear but at a higher seismic intensity of 0.9g, which is acceptable. This suggests that SSI delays damage progression, but requires greater deformation capacity. For extensive damage, the fixed-base behavior peaked at 3.81% drift and 8533 kN base shear at 1.2g PGA. The SSI-inclusive model attained this state at a higher PGA (1.5 g), recording a drift of 5.66% and base shear of 7979 kN. Notably, while the drift capacity increased, the base shear demand decreased slightly, reinforcing the role of SSI in redistributing seismic energy.

When the fixed-base model collapsed, it failed at a PGA of 1.3g, showing a drift of 4.07% and a base shear of 8864 kN. In contrast, the flexible-base system withstood up to 1.7 g PGA, achieving a drift of 6.31% and a similar base shear of 8734 kN. These findings suggest that while force resistance remains largely unchanged, incorporating SSI significantly enhances deformation capacity and delays system failure.

This behavior, although demonstrated using the Loma Prieta record, was consistent across a broader range of NFPL-GMs with LD. Table 11 summarizes the median threshold values for both drift and base shear across all damage states.

Figure 10 presents the fragility curves, developed using PGA, drift ratio, and base shear. The median capacity values, indicating a 50% probability of exceedance, are detailed in Table 12.

For NFPL-GMs with LD, incorporating SSI significantly altered the median capacity estimates across all the parameters. Compared to the fixed-base scenario, the PGA capacities increased by approximately 60% (slight), 45% (moderate), 33% (extensive), and 30% (collapse).

Table 11. Threshold values of EDPs for NFPL-GMs with LD

Base Condition	Damage State	Drift (%)	Base Shear (kN)
Fixed Base	Slight	0.76 – 1.98	3467.00 – 5504.80
	Moderate	1.98 – 3.92	5504.80 – 7523.10
	Extensive	3.91 – 5.40	7523.10 – 8591.00
	Collapse	5.40 & above	8591.00 & above
Flexible Base with SSI	Slight	1.55 – 4.62	3402.80 – 5354.00
	Moderate	4.62 – 7.20	5354.00 – 7345.10
	Extensive	7.20 – 8.73	7345.10 – 8536.90
	Collapse	8.73 & above	8536.90 & above

Table 12. Median capacities for NFPL-GMs with LD

Foundation	Parameters	PGA (g)	Drift (%)	Base Shear (kN)
Fixed	Slight	0.25	0.75	3484.50
	Moderate	0.55	1.82	5663.00
	Extensive	0.90	3.89	7285.50
	Collapse	1.15	4.94	8270.50
Flexible base with SSI	Slight	0.40	1.57	3400.00
	Moderate	0.80	4.68	5450.50
	Extensive	1.20	6.87	6961.50
	Collapse	1.50	8.89	8083.50

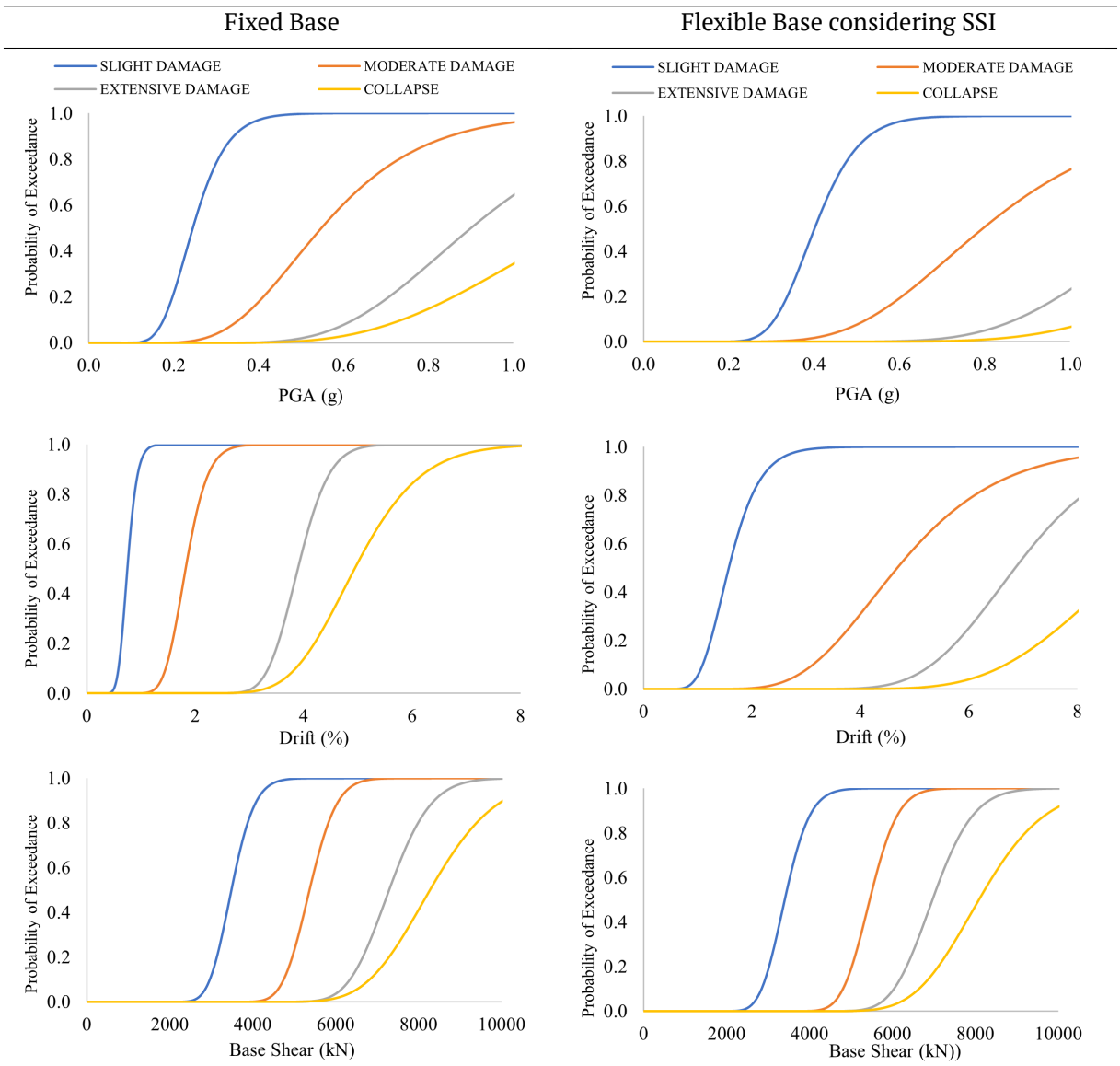

Figure 10 Fragility curves plotted against PGA, Drift and Base Shear for NFPL-GMs with LD.

The normalized drift capacities exhibited even more substantial increases, with changes of approximately 31% (slight), 77% (moderate), 32% (extensive), and 38% (collapse). In contrast, the base shear capacities exhibited relatively small variations, with increases of approximately 39% (slight), 34% (moderate), 28% (extensive), and 25% (collapse). It is important to note that both the drift and base shear were normalized with respect to PGA, as SSI directly increases the input motion intensity required to reach each damage state. Thus, normalization provides a consistent basis for comparison, highlighting the relative changes in deformation and force demands, independent of the absolute increase in GM intensity.

6.2 NFPL-GMs with HD

In evaluating NFPL-GMs with HD, the Superstition Hills-02 (RSN_723) record was selected for its distinctly high PGV/PGA ratio and pronounced velocity pulse characteristics. Figure 11 illustrates the IDA results for both base conditions under HD-GMs.

In Figure 12, under NFPL-GMs with HD, incorporating SSI consistently shifts the median capacities upward. Initially focusing on PGA, the flexible-base system required significantly higher intensity levels to reach equivalent limit states, with increases of 50% at slight damage, decreasing to 33% at moderate, 14% at extensive, and 12% at collapse.

Under slight damage conditions, the fixed-base system showed early signs of distress at 0.20g PGA, with a drift of 1.02% and a base shear of 2700 kN. In contrast, the flexible-base model (with SSI) reached this stage at 0.30g PGA, with a drift of 1.67% and a slightly lower base shear of 2660 kN. This pattern of delayed onset and increased drift was consistently observed. Moderate damage was recorded at 0.40g for the fixed-base system (1.78% drift, 4302 kN base shear) and at 0.60g for the flexible-base sys-

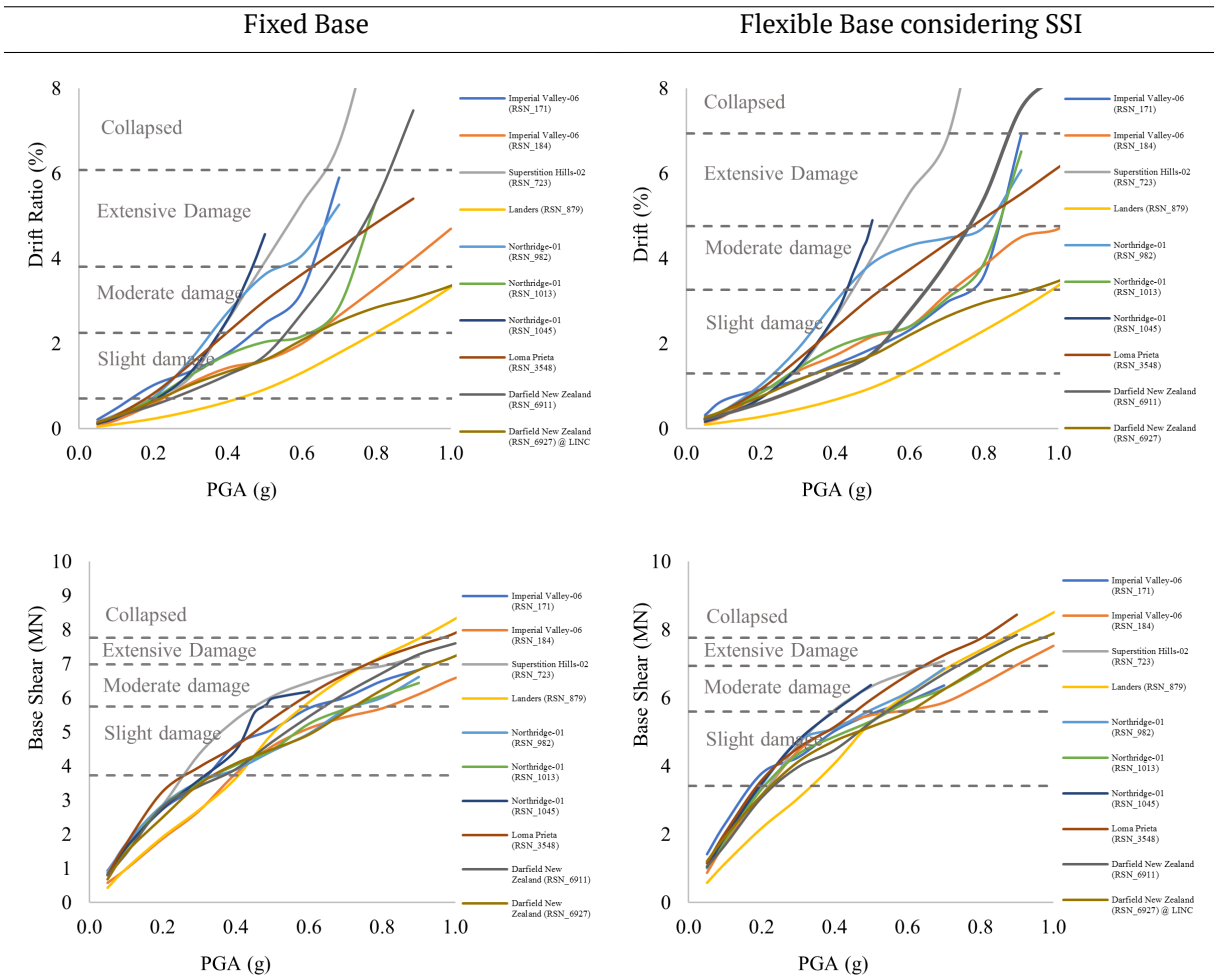

Figure 11 IDA curves of PGA versus drift and base shear under NFPL-GMs with HD.

tem (3.11% drift, 4870 kN base shear). At the extensive damage level, the fixed-base system exceeded a drift of 3.22% and a base shear of 7120 kN at 0.60g PGA, while the flexible-base system achieved a drift of 5.50% and a base shear of 6895 kN at 0.90g PGA. Although the base shear values remained comparable even at high seismic intensity, the flexible-base bridge demonstrated superior displacement tolerance.

In the fixed-base model, structural collapse occurred at a PGA of 0.70g, accompanied by a drift of 3.95% and a base shear of 8674.13 kN. In contrast, the flexible-base system withstood a PGA of 0.90 g, with a drift of 6.31% and a base shear of 7221 kN.

Compared to the LD case, these results suggest that HD motions accelerate damage progression; however, SSI still provides significant ductility benefits. Notably, the reduction in base shear observed under LD-GMs is less pronounced here, indicating that the intense pulse content of HD-GMs limits SSI's ability to redistribute force. Table 13 summarizes these threshold values across all states for HD. The

Table 13. Threshold values of EDPs for NFPL-GMs with HD

Base Condition	Damage State	Drift (%)	Base Shear (kN)
Fixed Base	Slight	0.71 – 2.25	3733.10 – 5742.00
	Moderate	2.25 – 3.81	5742.00 – 6981.30
	Extensive	3.81 – 6.08	6981.30 – 7770.50
	Collapse	6.08 & above	7770.50 & above
Flexible Base with SSI	Slight	1.30 – 3.27	3426.90 – 5596.00
	Moderate	3.27 – 4.76	5596.00 – 6944.10
	Extensive	4.76 – 6.94	6944.10 – 7761.40
	Collapse	6.94 & above	7761.40 & above

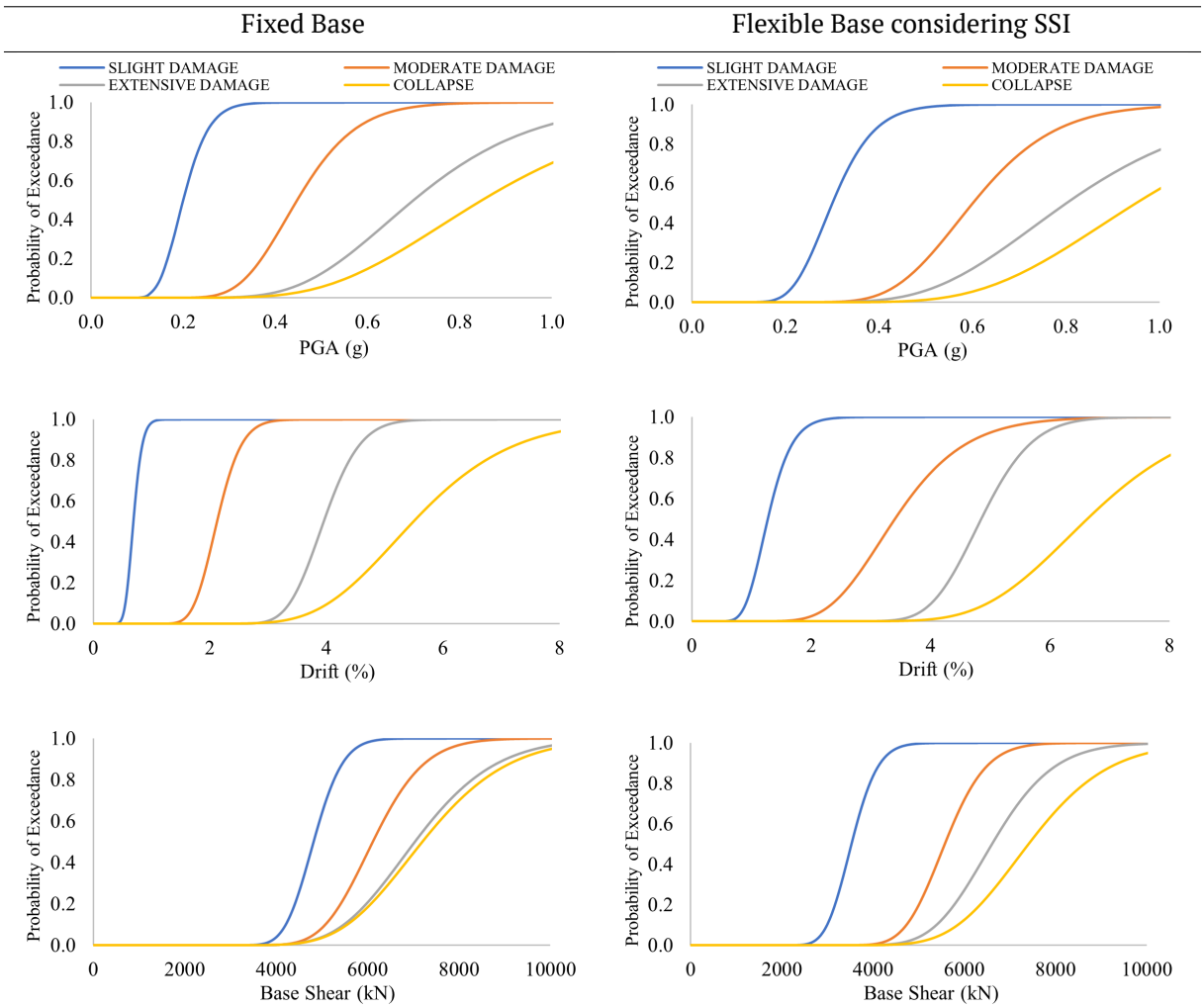

Figure 12 Fragility curves plotted against PGA, Drift and Base Shear for NFPL-GMs with HD.

fragility curves developed for this scenario further highlight these trends, with PGA and drift-based fragility curves showing significant shifts due to SSI.

This suggests that while SSI significantly delays the onset of damage, its influence wanes as the structure approaches failure. The effect on drift capacities follows a similar, though less pronounced, pattern. The normalized drift demands rose by approximately 24% at slight, 21% at moderate, and only around 7–8% at extensive and collapse, indicating that SSI enhances deformation capacity more notably in the early-to-moderate damage range than near ultimate failure. Conversely, variations in base shear remained relatively modest. The increases were 51% at slight, 32% at moderate, 18% at extensive, and 13% at collapse, confirming that SSI has a comparatively smaller impact on force demands than on deformation. It is important to emphasize that both drift and base shear were expressed in normalized form relative to PGA. Since SSI systematically elevates the input motion intensity at each damage state, normalization ensures that the comparisons capture the relative changes in structural response, independent of the absolute increase in GM demand. Table 14 provides a comprehensive summary of median capacity values across all EDPs. These findings underscore the ongoing significance of SSI in extending structural ductility, although designers should be aware of its limitations under strong PL excitations.

Table 14 presents the corresponding fragility-based median capacities. While drift and PGA medians show clear benefits from SSI, base shear capacities remain relatively close across both base conditions.

These trends underscore a key insight: SSI substantially improves drift-based performance and delays failure, but its influence on force-based metrics becomes marginal under forward directivity shaking. This is a critical consideration for NF bridge design, where displacement demands can quickly exceed conventional limits.

Although the case study highlights a typical bridge and soil profile characteristic of the chosen region, its findings have broader implications for assessing the seismic performance of bridges under soft to medium soil conditions worldwide. Notably, the significant increase in drift capacity and modest changes in base shear due to SSI, which may signifi-

Table 14. Median Capacities for NFPL-GMs with HD

Foundation	Parameters	PGA (g)	Drift (%)	Base Shear (kN)
Fixed	Slight	0.20	0.69	4814
	Moderate	0.45	2.12	6109
	Extensive	0.70	3.95	7029
	Collapse	0.85	5.49	7413
Flexible base with SSI	Slight	0.30	1.28	3529
	Moderate	0.60	3.41	5574
	Extensive	0.80	4.85	6611
	Collapse	0.95	6.62	7199

cantly affect the energy dissipation capability, align with mechanisms that may also affect bridges in other NF regions, such as California (USA), Turkey, Iran, Japan, and Italy, where soft soil basins and forward-directivity effects are common. Consequently, the outcomes of this study are not only regionally relevant, but also globally applicable, offering valuable insights for the seismic design and performance evaluation of bridges subjected to NFGMs in similar geotechnical environments.

7 CONCLUSIONS

This study presents a detailed seismic vulnerability assessment of an RC bridge subjected to NFPL-GMs, with focused attention on forward directivity effects and soil-structure interaction (SSI). Two categories of GMs were considered—LD and HD—defined based on PGV/PGA ratios. Analyses were performed using IDA for both fixed-base and flexible-base configurations, evaluating structural demand in terms of drift ratio and base shear.

Among the evaluated EDPs, base shear emerged as a particularly reliable and responsive metric—exhibiting strong correlation with PGA and displaying consistent trends across both foundation conditions. Its clear interpretability, coupled with its performance in regression analysis, reinforces its value as a primary response measure in seismic assessments. While base shear reductions due to SSI were moderate, they were measurable under LD-GMs, and the metric remained quite stable even as displacement demands increased under HD-GMs. This behavior highlights base shear's robustness for capturing force-level demands, particularly in NF contexts.

IDA results revealed that HD-GMs led to earlier damage and collapse at lower PGA levels, particularly in the fixed-base system. In contrast, the flexible-base bridge consistently demonstrated delayed damage progression and increased deformation capacity, especially under LD conditions. These results emphasize SSI's effectiveness in softening the seismic response and enabling higher drift capacity prior to failure.

Fragility analyses confirmed these trends. For LD-GMs, the flexible-base system showed normalized drift capacities up to 77% higher and normalized base shear increases of 25–39% compared to the fixed-base case. Under HD-GMs, SSI shifted normalized capacities upward, with drift gains of 21–24% at lower damage states but only 7–8% near collapse. Base shear variations remained modest (13–51%), indicating that SSI enhances deformation capacity more prominently than force demand when results are viewed in normalized terms. A comparative assessment between LD and HD fragilities showed that while both motion types induce similar damage mechanisms, HD-GMs trigger them more rapidly and at lower intensity. The performance gap between fixed and flexible systems narrows under HD shaking, reflecting limited time for SSI to manifest energy dissipation. In contrast, LD-GMs allow more gradual energy accumulation, enabling SSI to meaningfully improve both force and displacement behavior.

These findings highlight the critical need to account for both GM characteristics and foundation flexibility in seismic vulnerability studies. SSI should not be assumed to universally reduce demand; its effect is closely tied to the dynamic nature of input motions. Moreover, the use of multiple EDPs, such as drift and base shear, provides a more nuanced understanding of structural performance—capturing both ductility and strength responses. Ultimately, this research reinforces the value of integrated modeling in performance-based seismic design. For NF regions, especially those vulnerable to forward-rupture events with strong velocity pulses, ignoring directivity effects and SSI can result in underestimating vulnerability. A rigorous, multi-parameter assessment framework, as employed here, supports more resilient bridge design, targeted retrofitting strategies, and improved safety outcomes for critical infrastructure.

DISCLAIMER

The authors declare no conflict of interest.

REFERENCES

Ajom, B. and Bhattacharjee, A. (2017), Effect of earthquake on bridge foundation, *in* '13th International Conference on Vibration Problems (ICOVP)', Indian Institute of Technology Guwahati, India, pp. 1–13.
URL: *https://link.springer.com/book/10.1007/978-981-15-5862-7*

Akkar, S. and Moghimi, S. (2018), Implementation of near-fault forward directivity effects in seismic design codes, *in* 'Advances in Performance-Based Earthquake Engineering', Springer, pp. 183–201.
URL: *https://doi.org/10.1007/978-3-319-75741-4*$_7$

Alavi, B. and Krawinkler, H. (2004), 'Behavior of moment-resisting frame structures subjected to near-fault ground motions', *Earthquake Engineering & Structural Dynamics* **33**(6), 687–706.
URL: *https://doi.org/10.1002/eqe.369*

Alipour, A. and Zareian, F. (2008), Study rayleigh damping in structures: Uncertainties and treatments, *in* '14th World Conference on Earthquake Engineering (14WCEE)', Beijing, China. Paper No. 14_14-0243.
URL: *http://www.iitk.ac.in/nicee/wcee/article/14*$_1$$14 - 0243.PDF$

American Petroleum Institute (2007), 'Recommended practice for planning, designing and constructing fixed offshore platforms — working stress design'.
URL: *http://scholar.google.com/scholar?hl=enbtnG=Searchq=intitle:Recommended+Practice+for+planning,+designing+and+constructing+fixed+Offshore+Platforms+-+Working+stress+design*

Atefatdoost, G. R., Javidsharifi, B. and Shakib, H. (2018), 'Effects of foundation flexibility on seismic demands of asymmetric buildings subject to near-fault ground motions', *Structural Engineering and Mechanics* **66**(5), 637–648.
URL: *https://doi.org/10.12989/sem.2018.66.5.637*

Baig, M. A., Ansari, M. I., Islam, N. and Umair, M. (2023), 'Probabilistic damage analysis of isolated steel tub girder bridge excited by near and far fault ground motions', *International Journal of Engineering* **36**(2), 289–298.
URL: *https://www.ije.ir/article*$_1$$60838.html$

Baig, M. A., Ansari, M. I., Islam, N. and Umair, M. (2024), 'Probabilistic damage evaluation of isolated steel box-girder bridge excited by near-field earthquakes', *Soil Dynamics and Earthquake Engineering* **184**, 108869.
URL: *https://doi.org/10.1016/j.soildyn.2024.108869*

Baker, J. W. (2007), 'Quantitative classification of near-fault ground motions using wavelet analysis', *Bulletin of the Seismological Society of America* **97**(5), 1486–1501.
URL: *https://doi.org/10.1785/0120060255*

Bárcena, A. and Esteva, L. (2007), 'Influence of dynamic soil–structure interaction on the nonlinear response and seismic reliability of multistorey systems', *Earthquake Engineering & Structural Dynamics* **36**(3), 327–346.
URL: *https://doi.org/10.1002/eqe.633*

Behesthi Aval, S. B., Mohsenian, V. and Sadegh Kouhestani, H. (2018), 'Seismic performance-based assessment of tunnel form building subjected to near- and far-fault ground motions', *Asian Journal of Civil Engineering* **19**(1), 79–92.
URL: *https://doi.org/10.1007/s42107-018-0009-4*

Bi, K. and Hao, H. (2012), 'Modelling and simulation of spatially varying earthquake ground motions at sites with varying conditions', *Probabilistic Engineering Mechanics* **29**, 92–104.
URL: *https://doi.org/10.1016/j.probengmech.2011.09.002*

Billah, A. H. M. M., Alam, M. S. and Bhuiyan, M. A. R. (2013), 'Fragility analysis of retrofitted multicolumn bridge bent subjected to near-fault and far-field ground motion', *Journal of Bridge Engineering* **18**(10), 992–1004.
URL: *https://doi.org/10.1061/(ASCE)BE.1943-5592.0000452*

Bohara, B. K., Abdellatif, B., Deupa, J., Joshi, N. M. and Jagari, S. (2025), 'Seismic performance of reinforced concrete buildings in darchula, nepal: A fragility-based approach', *Journal of the Civil Engineering Forum* pp. 295–306.
URL: *https://doi.org/10.22146/jcef.21159*

Boulanger, R. W., Curras, C. J., Kutter, B. L., Wilson, D. W. and Abghari, A. (1999), 'Seismic soil-pile-structure interaction experiments and analyses', *Journal of Geotechnical and Geoenvironmental Engineering* **125**(9), 750–759.
URL: *https://doi.org/10.1061/(ASCE)1090-0241(1999)125:9(750)*

Bureau of Indian Standards (2016), Criteria for earthquake resistant design of structures, Technical Report December.
URL: *https://law.resource.org/pub/in/bis/S03/is.1893.1.2002.pdf*

Caltrans (2010), Caltrans seismic design criteria version 1.6, Technical report, California Department of Transportation, Sacramento, CA.
URL: *https://trid.trb.org/View/1248910*

Champion, C. and Liel, A. (2012), 'The effect of near-fault directivity on building seismic collapse risk', *Earthquake Engineering & Structural Dynamics* **41**(10), 1391–1409.
URL: *https://doi.org/10.1002/eqe.1188*

Chen, G., Yang, J., Wang, R., Li, K., Liu, Y. and Beer, M. (2023), 'Seismic damage analysis due to near-fault multipulse ground motion', *Earthquake Engineering & Structural Dynamics* **52**(15), 5099–5116.
URL: *https://doi.org/10.1002/eqe.4003*

Dreger, D., Hurtado, G., Chopra, A. and Larsen, S. (2011), 'Near-field across-fault seismic ground motions', *Bulletin of the Seismological Society of America* **101**(1), 202–221.
URL: *https://doi.org/10.1785/0120090271*

Fauzan, Z. A. J., Agista, G. A., Yokota, A. and Putra, M. E. (2025), 'Seismic and tsunamis vulnerability assessment of the shelter school building structure with and without retrofitting', *Journal of the Civil Engineering Forum* pp. 85–96.
URL: *https://doi.org/10.22146/jcef.13432*

FEMA356 (2000), Prestandard and commentary for the seismic rehabilitation of buildings, Technical report, Federal Emergency Management Agency.
URL: *https://www.nehrp.gov/pdf/fema356.pdf*

FEMA695 (2009), Quantification of building seismic performance factors, fema p695, Technical report, Applied Technology Council for the Federal Emergency Management Agency, Washington, D.C.
URL: *https://nehrpsearch.nist.gov/static/files/FEMA/fema$_p$695.pdf*

Gazetas, G. (1982), 'Shear vibration of vertically inhomogeneous earth dams', *International Journal for Numerical and Analytical Methods in Geomechanics* **6**(2), 219–241.
URL: *https://doi.org/10.1002/nag.1610060208*

Goodnight, J. C., Feng, Y., Kowalsky, M. J. and Nau, J. M. (2015), The effects of load history and design variables on performance limit states of circular bridge columns, Technical Report January, University of Alaska.
URL: *https://scholarworks.alaska.edu/handle/11122/10378*

Güllü, H. and Jaf, H. S. (2016), 'Full 3d nonlinear time history analysis of dynamic soil–structure interaction for a historical masonry arch bridge', *Environmental Earth Sciences* **75**(21), 1421.
URL: *https://doi.org/10.1007/s12665-016-6230-0*

Güllü, H. and Özel, F. (2020), 'Microtremor measurements and 3d dynamic soil–structure interaction analysis for a historical masonry arch bridge under the effects of near- and far-fault earthquakes', *Environmental Earth Sciences* **79**(13), 338.
URL: *https://doi.org/10.1007/s12665-020-09086-0*

Hokmabadi, A. S. and Fatahi, B. (2016), 'Influence of foundation type on seismic performance of buildings considering soil–structure interaction', *International Journal of Structural Stability and Dynamics* **16**(08), 1550043.
URL: *https://api.semanticscholar.org/CorpusID:109585949*

Huang, J. (2015), 'Earthquake damage analysis of concrete gravity dams: Modeling and behavior under near-fault seismic excitations', *Journal of Earthquake Engineering* **19**(7), 1037–1085.
URL: *https://doi.org/10.1080/13632469.2015.1027019*

Indian Roads Congress (2017), Irc6:2017, Technical report.
URL: *https://law.resource.org/pub/in/bis/irc/irc.gov.in.006.2017.pdf*

Izhar, M. S., Ansari, M. I. and Umair, M. (2024), 'Correction: Energy based seismic vulnerability assessment tool for reinforced concrete bridges', *Bulletin of Earthquake Engineering* **22**(11), 5951–5951.
URL: *https://doi.org/10.1007/s10518-024-01986-x*

Jiang, L., Zhong, J. and Yuan, W. (2020), 'The pulse effect on the isolation device optimization of simply supported bridges in near-fault regions', *Structures* **27**, 853–867.
URL: *https://doi.org/10.1016/j.istruc.2020.06.034*

Kabir, M. R., Billah, A. H. M. M. and Alam, M. S. (2019), 'Seismic fragility assessment of a multi-span rc bridge in bangladesh considering near-fault, far-field and long duration ground motions', *Structures* **19**, 333–348.
URL: *https://doi.org/10.1016/j.istruc.2019.01.021*

Lai, Z., Jiang, L., Chen, Y. and Wei, B. (2024), 'An improved model for the nonlinear simulation of the high-speed vehicle-track-bridge coupling system under seismic shaking', *Earthquake Engineering & Structural Dynamics* **53**(12), 3775–3797.
URL: *https://doi.org/10.1002/eqe.4196*

Li, S., Zhang, F., Wang, J., Alam, M. S. and Zhang, J. (2017), 'Effects of near-fault motions and artificial pulse-type ground motions on super-span cable-stayed bridge systems', *Journal of Bridge Engineering* **22**(3).
URL: *https://doi.org/10.1061/(ASCE)BE.1943-5592.0001008*

Mallick, M. and Raychowdhury, P. (2015), 'Seismic analysis of highway skew bridges with nonlinear soil–pile interaction', *Transportation Geotechnics* **3**, 36–47.
URL: *https://doi.org/10.1016/j.trgeo.2015.03.002*

Mangalathu, S., Jeon, J.-S. and Jiang, J. (2019), 'Skew adjustment factors for fragilities of california box-girder bridges subjected to near-fault and far-field ground motions', *Journal of Bridge Engineering* **24**(1).
URL: *https://doi.org/10.1061/(ASCE)BE.1943-5592.0001338*

Moniri, H. (2017), 'Evaluation of seismic performance of reinforced concrete (rc) buildings under near-field earthquakes', *International Journal of Advanced Structural Engineering* **9**(1), 13–25.
URL: *https://doi.org/10.1007/s40091-016-0145-6*

Naeim, F. and Kelly, J. M. (1999), *Design of Seismic Isolated Structures: From Theory to Practice*, John Wiley & Sons, Inc., New York.
URL: *https://www.wiley.com/en-us/Design+of+Seismic+Isolated+Structures:From+Theory+to+Practice-p-9780471149217*

Najar, I. A., Ahmadi, R., Amuda, A. G., Mourad, R., Bendary, N. E., Ismail, I., Bakar, N. A. and Tang, S. (2025), 'Advancing soil-structure interaction (ssi): a comprehensive review of current practices, challenges, and future directions', *Journal of Infrastructure Preservation and Resilience* **6**(1), 5.
URL: *https://doi.org/10.1186/s43065-025-00118-2*

Pacific Earthquake Engineering Research Center (1999), 'Strong motion database'.
URL: *http://ngawest2.berkeley.edu*

Padgett, J. E., Nielson, B. G. and DesRoches, R. (2008), 'Selection of optimal intensity measures in probabilistic seismic demand models of highway bridge portfolios', *Earthquake Engineering & Structural Dynamics* **37**(5), 711–725.
URL: *https://doi.org/10.1002/eqe.782*

Paudel, S., Maulana, T. I., M., I. and Prayuda, H. (2024), 'Seismic vulnerability assessment of regular and vertically irregular residential buildings in nepal', *Journal of the Civil Engineering Forum* pp. 199–208.
URL: *https://doi.org/10.22146/jcef.10316*

Paulay, T. and Priestley, M. J. N. (1992), *Seismic Design of Reinforced Concrete and Masonry Buildings*, 2nd edn, John Wiley and Sons, New York.
URL: *https://www.researchgate.net/publication/338551990_Seismic_design_of_reinforced_concrete_and_masonry_buildings*

Roeder, C. W., Stanton, J. F. and Taylor, A. W. (1987), Performance of elastomeric bearings, Technical Report 298, National Cooperative Highway Research Program, Transportation Research Board, National Research Council, Washington, D.C.
URL: *https://onlinepubs.trb.org/Onlinepubs/nchrp/nchrp$_{rpt}$298.pdf*

Sharma, V., Shrimali, M. K., Bharti, S. D. and Datta, T. K. (2021), 'Seismic fragility evaluation of semi-rigid frames subjected to near-field earthquakes', *Journal of Constructional Steel Research* **176**, 106384.
URL: *https://doi.org/10.1016/j.jcsr.2020.106384*

Spagnuolo, E., Akinci, A., Herrero, A. and Pucci, S. (2016), 'Implementing the effect of the rupture directivity on psha for the city of istanbul, turkey', *Bulletin of the Seismological Society of America* **106**(6), 2599–2613.
URL: *https://doi.org/10.1785/0120160020*

Takeda, T., Sozen, M. A. and Nielsen, N. N. (1970), 'Reinforced concrete response to simulated earthquakes', *Journal of the Structural Division* **96**(12), 2557–2573.
URL: *https://doi.org/10.1061/JSDEAG.000276*

Visuvasam, J. and Chandrasekaran, S. S. (2019), 'Effect of soil–pile–structure interaction on seismic behaviour of rc building frames', *Innovative Infrastructure Solutions* **4**(1), 45.
URL: *https://doi.org/10.1007/s41062-019-0233-0*

Xiong, W., Jiang, L.-Z. and Li, Y.-Z. (2016), 'Influence of soil–structure interaction (structure-to-soil relative stiffness and mass ratio) on the fundamental period of buildings: experimental observation and analytical verification', *Bulletin of Earthquake Engineering* **14**(1), 139–160.
URL: *https://doi.org/10.1007/s10518-015-9814-2*

Yang, D., Pan, J. and Li, G. (2009), 'Non-structure-specific intensity measure parameters and characteristic period of near-fault ground motions', *Earthquake Engineering & Structural Dynamics* **38**(11), 1257–1280.
URL: *https://doi.org/10.1002/eqe.889*

Yu, J., Jiang, L., Zhou, W., Liu, X., Lai, Z. and Feng, Y. (2022), 'Study on the dynamic response correction factor of a coupled high-speed train–track–bridge system under near-fault earthquakes', *Mechanics Based Design of Structures and Machines* **50**(9), 3303–3321.
URL: *https://doi.org/10.1080/15397734.2020.1803753*

Zhai, C., Chang, Z., Li, S., Chen, Z. and Xie, L. (2013), 'Quantitative identification of near-fault pulse-like ground motions based on energy', *Bulletin of the Seismological Society of America* **103**(5), 2591–2603.
URL: *https://doi.org/10.1785/0120120320*

Zhan, P., Xue, S., Li, X., Sun, G. and Ma, R. (2024), 'Seismic assessment of large-span spatial structures considering soil–structure interaction (ssi): A state-of-the-art review', *Buildings* **14**(4), 1174.
URL: *https://doi.org/10.3390/buildings14041174*